Chapter 18
X-Band Synthetic Aperture Radar Methods

Saverio Mori, Frank S. Marzano, and Nazzareno Pierdicca

Abstract Spaceborne Synthetic Aperture Radars (SARs), operating at L-band and above, offer microwave observations of the Earth at very high spatial resolution in almost all-weather conditions. Nevertheless, precipitating clouds can significantly affect the signal backscattered from the ground surface in both amplitude and phase, especially at X band and beyond. This evidence has been assessed by numerous recent efforts analyzing data collected by COSMO-SkyMed (CSK) and TerraSAR-X (TSX) missions at X band. This sensitivity can be exploited to detect and quantify precipitations from SARs at the spatial resolution of a few hundred meters, a very appealing feature considering the current resolution of precipitation products from space. Forward models of SAR response in the presence of precipitation have been developed for analyzing SAR signature sensitivity and developing rainfall retrieval algorithms. Precipitation retrieval algorithms from SARs have also been proposed on a semi-empirical basis. This chapter will review experimental evidences, modelling approaches, retrieval methods and recent applications of X-band SAR data to rainfall estimation.

Keywords Synthetic aperture radar · High resolution · Clouds · Rainfall · Precipitation · Raindrops · Snowflakes · Reflectivity · Normalized radar cross section · Particle size distribution · Polarization · Regressive empirical algorithm · Probability matching algorithm · COSMO-SkyMed · TerraSAR-X

18.1 Introduction

The importance of monitoring global precipitations and their associated extreme events, such as floods, landslides, hurricanes, and droughts, is crucial for the management of daily life and environmental crises (Skofronick-Jackson et al.

S. Mori (✉) · F. S. Marzano · N. Pierdicca
Department of Information Engineering, Electronics and Telecommunications, University of Roma "La Sapienza", Rome, Italy
e-mail: saverio.mori@uniroma1.it

V. Levizzani et al. (eds.), *Satellite Precipitation Measurement*, Advances in Global Change Research 67, https://doi.org/10.1007/978-3-030-24568-9_18

2017). Global-scale precipitation measurements are essential for the development and validation of both weather and climate models (Ebert et al. 2007). Cloud-resolving models require global, kilometer-scale observations to provide diagnoses of their performance and to develop adequate data assimilation procedures (e.g., Masunaga et al. 2008).

Since the 1980s much of our understanding of global precipitation has been provided by spaceborne passive microwave radiometers (e.g., Kummerow et al. 1998; Marzano et al. 2002; Skofronick-Jackson et al. 2017). Precipitation retrievals from microwave radiometer data over land is affected by a low spatial resolution, typically larger than tens of kilometers. Spaceborned infrared radiometers can offer an adequate resolution of few kilometers, but they are nearly saturated by the presence of precipitating clouds within the observed scene. Space-based weather radars, operating at Ku band (i.e., about 2-cm wavelength) and beyond, have represented a key advance in satellite precipitation monitoring. The Ku-band Precipitation Radar (PR) aboard the Tropical Rainfall Measurement Mission (TRMM) satellite has provided unprecedented and unique precipitation measurements over land, even though limited by a swath smaller than microwave radiometers (Kummerow et al. 1998). The development and launch of the Global Precipitation Measurement (GPM) mission has further advanced spaceborne radar technology by means of the Dual-Frequency Precipitation Radar (DPR) at Ku and Ka band (Hou et al. 2014). However, if significant shallow precipitation or rain cells smaller than few kilometers occur over land, then both PR and DPR may miss or underestimate the intensity of such precipitation fields (e.g., Marzano et al. 2011; Durden et al. 1998).

The high spatial resolution of Synthetic Aperture Radars (SARs) at X band (i.e., about 3 cm wavelength) and beyond can provide new insights into the structure of precipitating clouds and permit the observation of small precipitation cells at micro-alpha scale (between 0.2 and 2 km). Indeed, the nominal spatial resolution of SAR is of the order of meters, but it is degraded to hundreds of meters by the turbulent motion of the hydrometeors due the random broadening of the Doppler-frequency spectra with respect to fixed-target surface imaging (Atlas and Moore 1987). Spaceborne SARs at C-band and L-band (i.e., about 5 and 21 cm wavelengths, respectively) have a long heritage for Earth observation, but these space radars are relatively insensitive to rainfall. Space Shuttle missions in 1994 and 2000 carried the first X-band SAR (X-SAR) along with L-band and C-band SARs (Jordan et al. 1995). Since then, the possibility of detecting and quantifying precipitation from SARs has received more attention (e.g., Alpers and Melsheimer 2004; Atlas and Moore 1987; Ferrazzoli and Schiavon 1987; Melsheimer et al. 1998; Moore et al. 1997). In the last decade, new X-SARs such as four COSMO-SkyMed (CSK) satellites (ASI 2009) and two TerraSAR-X (TSX) satellites (Fritz and Eineder 2013) followed by other missions such as TecSAR and KOMPSAT-5 have been succesfully launched. First analyses of X-band SAR influence of precipitating clouds date back to the ‘80s (Atlas and Moore 1987).

Precipitating clouds can significantly alter the specabeorne backscattered SAR signal, introducing path attenuation and scattering as well as depolarization and

tropospheric scintillation (Ferrazzoli and Schiavon 1987; Quegan and Lamont 1986; Alpers and Melsheimer 2004). An extensive review of the atmospheric impacts on the retrieved TSX data, can be found in Weinman and Marzano (2008) and Danklmayer et al. (2009). The latter analyze a large dataset of TSX acquisitions finding evident precipitations effects in only 0.8% of cases. The analyzed cases confirm the effect of precipitation on X Band SAR data, but also have provided evidence that only intense events can produce significant effects at X band. Synergy and complementarity of X-band SAR with ground-based weather radars have been investigated in Marzano et al. (2010) and Fritz and Chandrasekar (2010, 2012). A forward model is generally needed to convert weather radar reflectivity into spaceborne SAR path attenuation and signal, taking into account polarimetric features as well (Marzano et al. 2012). Several steps are necessary to simulate a X-band SAR precipitation signature using weather radar (WR) reflectivity: (1) estimation of the specific differential phase; (2) path attenuation correction (if necessary); (3) gridding on an Earth-centric Cartesian grid; (4) hydrometeor classification, in order to use the correct particle distribution model; (5) scale frequency and look angle; (6) SAR geometry resampling and (7) integration to SAR observations. Obtainable polarimetric products include the differential reflectivity, and the differential phase, simulated at both X band and Ku band. Baldini et al. (2014) have carried out a review of the model of Fritz and Chandrasekar (2012) adding formulas for simulating X-band SAR observables from ground weather radar reflectivity at C and S band. An analysis of the CSK Ping-Pong mode (alternate HH-VV) was also carried out, showing some interesting features. Roberto et al. (2014) extend this model approach to marine environments, a fairly challenging goal due to the difficulties in modelling the SAR response of the sea surface background. The detection of the hurricane eye, hurricane tracking, and the estimation of wind fields from SAR data has also been recently attempted (Li 2017). Hydrological applications of X-band SARs are typically oriented to flood monitoring (e.g., Landuyt et al. 2018; Refice et al. 2018), but precipitation effects can be quantified as well (Marzano et al. 2011).

This chapter aims to provide an overview of X-band SAR techniques for precipitation signature characterization and detection, introducing both precipitation response simulations (forward models) and precipitation retrieval methods (inverse models). Sect. 18.2 shows an example of precipitation signatures on SAR imagery, whereas Sect. 18.3 describes a forward model of SAR response in the presence of precipitation. Section 18.4 illustrates some precipitation retrieval techniques used in literature, whereas Sect. 18.5 deals with an advanced approach and the applications of validation techniques. Finally, Sect. 18.6 contains a discussion on high-frequency SAR for hydrological applications and future perspectives.

18.2 Evidence of Precipitation Signatures on X-SAR Imagery

In Marzano et al. (2010) several examples of precipitation SAR signatures at X band are discussed. A very good example is represented by Hurricane Gustav, observed by TerraSAR-X (TSX) on 2 September 2008, from 11:58:44 to 11:59:06 UTC, a few hours after landfall on the US coast. The selected case study refers to the passage of Hurricane Gustav over Louisiana and Mississippi northwestward, moving at an average velocity of 24 km h^{-1} and delivering torrential rains to the central gulf coast of the US (e.g., Larto Lake, LA, reported a rainfall total accumulation of 533.4 mm). Ideally speaking, atmospheric effects could be detected, or at least appreciated, using a clear-sky image acquired by the same instrument in the same transmitting and receiving polarization and the same acquisition mode, and orbit direction, during a recent date. Such images are referred to as "SAR background images". Unfortunately, in this case no background image was available.

Figure 18.1 shows the synoptic view of an outer rain band of Hurricane Gustav over south-eastern Louisiana taken from the NEXRAD ground Weather Radar (WR) located in Mobile (Alabama) (e.g., Fulton et al. 1998). WR acquisition started at 11:59:44 UTC so the time difference with TSX is about 1 min. From the radiosonde available from Birmingham (AL) at 12:00 UTC, the freezing level height was about 4.5 km. The white box shows precipitation around 30.5° N × 89.5° W. The near-surface conical scan at 0.86° elevation angle and HH-polarized of NEXRAD rainfall data is compared to the ScanSAR map of TSX HH-polarized Normalized Radar Cross Section (NRCS) observation. Note that TSX ScanSAR product has a ground coverage of 154 × 105 km^2 and a ground resolution of about 18 × 18 m^2. WR reflectivity has a spatial resolution of about 0.25 km in range and 0.5° in azimuth and nominal coverage radius of about 209 km. In the previous figure it is evident that the correspondence over land between WR higher reflectivity areas and TSX dark ones. TSX returns over ocean are also detectable by a brighter incoherent feature with respect to the darker quasi-specular NRCS response, due to the sea surface. The southern portion of the rain band over ocean corresponds to WR reflectivity of about 20 dBZ. Values of Z are as high as 59.1 dBZ, indicating torrential convective rainfall connected to Hurricane Gustav, probably mixed with some hail.

The correlation between NRCS values σ_{SAR} [dB] (filtered and resampled) against co-located and co-registered WR reflectivity Z [dBZ] for a central Region of Interest (ROI) is shown in Fig. 18.2. The co-polar radar reflectivity factor Z is proportional to the radar reflectivity η of the WR through $Z = \eta\lambda^4/(\pi^5|K|^2)$ with λ the wavelength and $|K|^2$ the dielectric factor equal to 0.93 for water (Bringi and Chandrasekar 2001). A significant negative correlation is present between X-Band σ_{SAR} and S-band Z, demonstrating that the X-SAR NRCS tends to decrease as the S-band WR reflectivity increases, mainly due to the increase of two-way rain path attenuation. The dynamic range of X-SAR NRCS due to rainfall is about 12 dB. Moreover, X-SAR NRCS tends to saturate for values of S-band Z of about 25 dBZ and below.

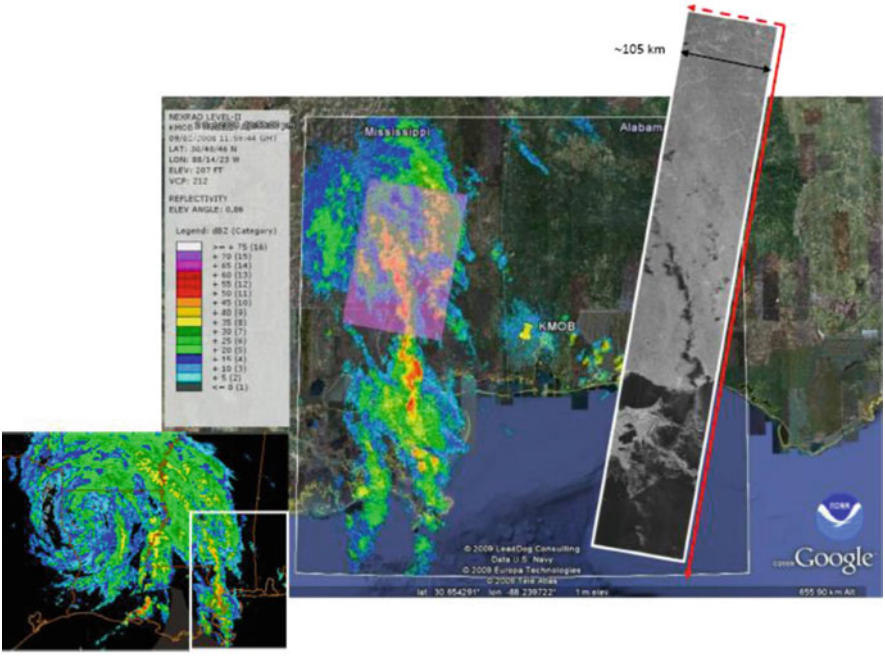

Fig. 18.1 (Lower left image) Synoptic view of Hurricane Gustav over south eastern Louisiana on September 2, 2008 12:00 UTC taken from NEXRAD weather radar reflectivity mosaic. The white box shows an outer rain band around 30.5° N × 89.5° W. (Central image) Geographic representation of the NEXRAD image at 0.86° elevation, acquired by the S-band radar (KMOB, in figure) near Mobile (Alabama). The semi-transparent rectangular box represents the scene of interest, acquired by TSX X-SAR on 2 September 2008 12:00 UTC in HH polarization and ScanSAR mode (100 km swath). (Upper right image) TSX quicklook of the acquisition in arbitrary units at 100-m resolution; flight direction is indicated. (Adapted from Marzano et al. 2010)

The dispersion between σ_{SAR} and Z is mainly due to the slant-view observation geometry, surface NRCS variability and the spatial inhomogeneity of hydrometeor distribution. The trend of this curve is similar to the one indicated in Fritz and Chandrasekar (2010).

The Tropical Rainfall Measuring Mission (TRMM) satellite observed the area at about 15:30 UTC of 2 September 2008. The significant time-difference makes a direct comparison with TSX data impractical. Nevertheless, the TRMM acquisition allows a qualitative comparison with MW radiometric and radar spaceborne imagers. In this respect, the principal TRMM instruments are the TRMM Microwave Imager (TMI), a passive microwave sensor, and the Precipitation Radar (PR), an active one. Figure 18.3 shows the acquired horizontally polarized TMI brightness temperatures (TB) at 37 GHz and 85.5 GHz (obtained from TRMM 1B11 product). The TMI image swath is about 760 km wide, while the ground resolution is about 16×9 km^2 at 37 GHz and 7×5 km^2 at 85.5 GHz. The hurricane signature is quite evident, but

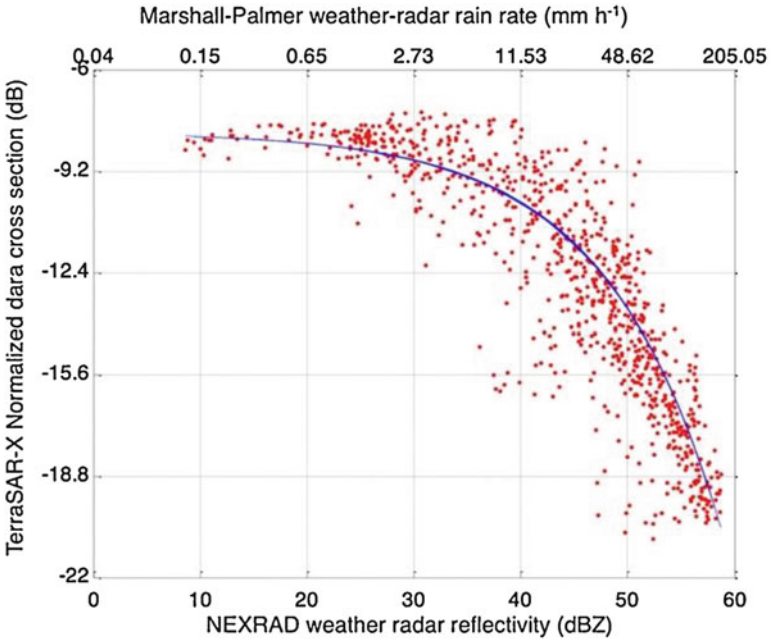

Fig. 18.2 Correlation diagram between NRCS values X-band σSAR against co-located and co-registered S-band NEXRAD weather-radar reflectivity Z, for a selected region of interest (ROI) of the scene. The upper axis provides the estimated rain-rate from NEXRAD data using the Marshall-Palmer relation (Bringi and Chandrasekar 2001). The best-fitting curve is also plotted. (Adapted from Marzano et al. 2010)

the impact of the different spatial resolution between the two radiometric channels is also striking. Figure 18.3 also illustrates the PR reflectivity factor (dBZ) at 14 GHz closest to the surface for both the "normal sampled" range bin 75 and the "rain oversampled" range bin 16 (as obtained from TRMM 1C21 product). The PR swath is 220 km for the "normal sampled" product, but it is reduced for the "rain oversampled" one due to oversampling; the height resolution is about 250 m. The "rain oversampled" product aims at registering the detailed vertical profile of the rain. The spiral bands of the hurricane are detectable with a moderate spatial resolution, but only the combination with TMI can provide the general features of the hurricane due to the relatively smaller swath. Spaceborne microwave radiometers (passive instruments) allow a wider swath, but with a rougher resolution with respect to radars (active instruments). Note that the radar resolution is coarser than the SAR, but the vertical ranging allows for atmospheric profiling, a feature not possible for SAR due to their slant observing geometry and surface-tuned receiving time-window (Marzano et al. 2011).

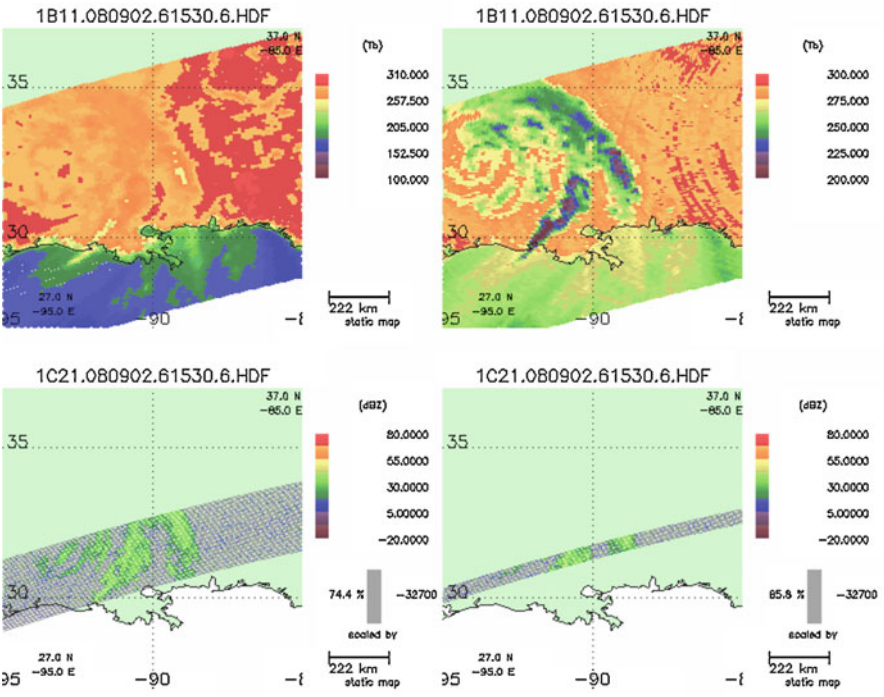

Fig. 18.3 TRMM observations, at 15:30 UTC, for the case study of Hurricane Gustav. (Top panels) TRMM 1B11 brightness temperature (TB) product relative to TMI channel 7 (37 GHz horizontal polarization, left), beam effective field-of-view (EFOV) of 16×9 km^2, and TMI channel 9 (85.5 GHz horizontal polarization, right) with a main-beam EFOV of 7×5 km^2. The cyclonic cell indicated in Fig. 18.2 is well captured. (Bottom panels) The TRMM 1C21 radar reflectivity (dBZ) product, relative to PR normal sample (left) range bin 75, and PR rain oversampled (right), range bin 16. Note that the PR swath is 220 km wide (reduced in the oversampled product) and the range resolution is 0.25 km; TMI swath is 760 km wide. (Adapted from Marzano et al. 2011)

18.3 Forward Model of SAR Response to Rainfall

Polarimetric radars are powerful tools for quantitative studies of the properties of atmospheric hydrometeors (e.g., Bringi and Chandrasekar 2001; Doviak and Zrnić 1993). Conventional radars measure the backscattered intensity from hydrometeors in a scattering volume defined by the antenna-beam width and the transmitted-pulse width. For a polydispersion of oblate ellipsoidal particles, with a random distribution of spherical volume-equivalent diameter D and zenithal canting angle ϕ, being λ the wavelength corresponding to a frequency f, we can define several RADAR observables related to the incoming signal power. In particular, η_{pq} is the pq-polarized radar reflectivity (in km^{-1}, or backscattering cross section per unit of volume) and can be expressed in terms of Particle Size Distribution (PSD) $N(D)$, particle orientation density $p_o(\phi)$ and the complex backscattering matrix element $S_{pq}(D, \phi)$. Instead of

reflectivity, radar reflectivity factors Z_{hh}, Z_{vv} and Z_{vh} (in mm^6 m^{-3} or dBZ) can be used. Note that the double subscript stands for the received (first index) and transmitted (second index) polarization state, which can be either horizontal (h) or vertical (v). K_{dp} is the specific differential phase shift (in $^\circ$ km^{-1}) due to the forward propagation phase difference between the two polarizations. k_{pp} is the specific power attenuation at polarization p in km^{-1} (or A_{pp} if expressed in dB km^{-1}) and is the counterpart of K_{dp} in terms of power attenuation per unit length.

Given a volumetric distribution of atmospheric water particles, radar observables can be used to estimate the SAR signal when observing ground targets in the presence of atmospheric effects by means of a SAR response forward model. The next section illustrates the model proposed in Marzano et al. (2012) and Mori et al. (2017a).

18.3.1 SAR Observing Geometry and Response Model

The fundamental parameter, imaged by SARs, is the Radar Cross Section (RCS) σ_{pq} of the target, defined by $P_p = \sigma_{pq} \cdot S_q^i / 4\pi$, where P_p is the power re-irradiated by the target at polarization p and $S_q^{\,i}$ is the incident power density at polarization q (Ulaby and Long 2014). While the previous definition corresponds to point targets, NRCS (also indicated as backscattering coefficient $\sigma_{pq}{}^0$) is usually defined as the RCS normalized to the target area A for distributed targets, that is $\sigma_{pq}{}^0 = \sigma_{pq}/A$.

In the presence of precipitation, the SAR backscattering response has to account for the two-way attenuation of the surface echo due to the atmospheric particles, the atmospheric volume reflectivity and phase shift.

We can express the spaceborne SAR co-polar and cross-polar NRCS for a given pixel with coordinates (x,y) on the Earth surface, using a simplified model where the forward depolarization is neglected and the isorange lines, actually spherical, are supposed to be planar as shown in Fig. 18.4:

$$\sigma^0_{SARpq}(x,y) = 4\pi \left\langle \left| S_{SARpq} \right|^2 \right\rangle = \sigma^0_{SRFpq}(x,y) + \sigma^0_{VOLpq}(x,y) \tag{18.1}$$

$$\sigma^0_{SRFpq}(x,y) = \sigma^{0ground}_{pq}(x,y)\, exp\left(- \int\limits_{\Delta l(x,y)} k_{qq}(l)dl - \int\limits_{\Delta l(x,y)} k_{pp}(l)dl \right)$$

$$\sigma^0_{VOLpq}(x,y) = \sin(\theta) \int\limits_{\Delta t(x,y)} \eta_{pq}(t) \exp\left(- \int\limits_{\Delta l(t)} k_{qq}(l)dl - \int\limits_{\Delta l(t)} k_{pp}(l)dl \right) dt$$

where θ is the local incident angle, and S_{SARpq} are the elements of the SAR received backscattering matrix. $\sigma^0{}_{SRFpq}(x,y)$ (in m^2 m^{-2}) is the "surface-driven" backscattering coefficient, that is the surface target NRCS $\sigma^{0ground}{}_{pq}$ (superscript "ground" here

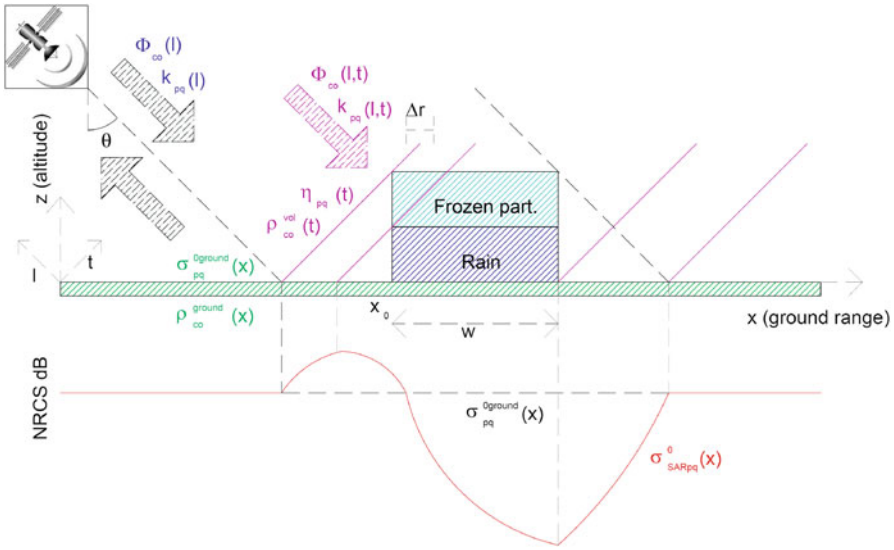

Fig. 18.4 Schematic SAR NRCS (in dB) as a function of cross-track scanning distance x, showing enhanced values on the left of the cross-over point caused by scattering from the cloud top and attenuation from rain in the lower cloud on the right. The viewing angle with respect to nadir (incidence angle) is θ, while the cloud extension is w. The symbol Δr indicates the width of the slant slice of the atmosphere representing the SAR side-looking resolution volume. The figure also shows the energy fluxes and the e.m. parameters of the model according to Marzano et al. (2012) and Mori et al. (2017a)

refers to the surface target property) attenuated by the two-way path through the precipitating atmosphere, whereas the term $\sigma^0_{VOLpq}(x,y)$ ($m^2\ m^{-2}$) is the "volume-driven" backscattering due to hydrometeor reflectivity, weighted by the two-way path through the precipitating atmosphere. The spatial transverse coordinates l and t along the atmospheric path (in km), inherently depend on the Cartesian coordinate in the volume (x,y,z). The path from the radar to the surface target at (x,y) is $\Delta l(x,y)$. Note that the volume term accounts for the contributions to the SAR echo due to the atmospheric hydrometeors encountered by the path-attenuated SAR wave front aligned along the transverse coordinate t and in the same resolution cell Δr. The scattered wave from hydrometeors, encountered at position t along the transverse line, experiences an attenuation along the path $\Delta l(t)$ when propagating back to the radar. The SAR model geometry, shown in Fig. 18.4, depicts a possible enhancement of the background response at near range, due to frozen particle scattering at high altitudes, followed by an intense attenuation of the background signal, due to the path attenuation through the rain cloud. This pattern is evident in the case of Fig. 18.4.

Spaceborne satellite SARs usually allow the observation of the co-polar elements of the 3×3 ensemble-average scattering covariance matrix $\mathbf{C}_{\mathrm{SAR}}$. Operational SAR systems may allow the measurement of the cross-polar elements, whereas co-polar backscattering coefficients are always available. We can define the following SAR

polarimetric observables (e.g., Bringi and Chandrasekar 2001; Marzano et al. 2012; Ulaby and Elachi 1990):

$$\sigma_{SARppqq}(x,y) = 4\pi\left\langle S_{SARpp}(x,y)S^{*}_{SARqq}(x,y)\right\rangle \tag{18.2}$$

$$\sigma_{SARpq}(x,y) = 4\pi\left\langle S_{SARpq}(x,y)S^{*}_{SARpq}(x,y)\right\rangle \tag{18.3}$$

$$Z_{SARco}(x,y) = \frac{\sigma_{SARhh}(x,y)}{\sigma_{SARvv}(x,y)} \tag{18.4}$$

$$\rho_{SARco}(x,y) = \frac{S_{SARvv}(x,y)S^{*}_{SARhh}(x,y)}{\sqrt{|S_{SARhh}(x,y)|^2}\sqrt{|S_{SARvv}(x,y)|^2}} = |\rho_{SARco}(x,y)|\, exp\,(j\Psi_{SARco}(x,y)) \tag{18.5}$$

where σ_{SARpq} is the pq-polarized NRCS (or backscattering coefficient, adimensional), and σ_{SARhv} the cross-polarizations and σ_{SARhh}, σ_{SARvv} the co-polarizations. The term $\sigma_{SARppqq}$ describes the cross term among orthogonal polarizations. Z_{SARco} is the co-polar ratio (or difference, if expressed in decibels), whereas ρ_{SARco} is the complex correlation coefficient (or degree of correlation, adimensional), expressed by an amplitude $|\rho_{SARco}|$ and a phase Ψ_{SARco}.

When dealing with the co-polar differential phase, the SAR polarimetric phase model needs to account for the slant observing geometry within a precipitation medium (see Fig. 18.4). In clear sky the SAR phase response is given by the ground polarimetric differential phase, indicated by $\delta^{0}_{co}(x,y)$, due to the surface interaction. The path through the hydrometeors adds a two-way rotation along the incident path, given by the path integral of the specific differential phase $K_{co}(x,y,z)$ (propagation phase shift). The precipitation-cell backscatter also introduces a differential phase, $\delta_{co}(t)$, i.e. the phase rotation between S_{hh} and S_{vv} of the scattering volume (depending on the cell position, t), additionally affected by the 2-way path from the same volume to the radar (Bringi and Chandrasekar 2001; Marzano et al. 2012). According to Matrosov et al. (1999), values of δ_{co} are small for S-band wavelengths even for intense rainfall rates; however, at X band it is negligible only for modest precipitation rates, wheras at Ka band values, δ_{co} can be very significant even for modest rainfall rates. A formulation of the observable SAR complex correlation coefficient for a ground point (x,y) is presented in Marzano et al. (2012) and revised in Mori and Marzano (2017a) in the form:

$$\rho_{SARco}(x,y) = \frac{f(\sigma^{0ground}_{vv}, \sigma^{0ground}_{hh}, \rho^{0}_{co}) \cdot L(k_{hh}, k_{hh}, K_{co}) + \sin(\theta)\int_{\Delta t} C_{vol}(t)dt}{f'(\sigma_{SARhh}, \sigma_{SARvv})} \tag{18.6}$$

$$C_{vol}(t) = f''(\eta_{hh}, \eta_{hh}, \rho_{co}) \cdot L(k_{hh}, k_{hh}, K_{co})$$

where $\rho^0_{co}(x,y) = \left|\rho^0_{co}(x,y)\right| exp\left(j\delta^0_{co}(x,y)\right)$ is the complex correlation coefficient of the ground target and $\rho_{co}(x,y) = |\rho_{co}(x,y)| exp\ (j\delta_{co}(x,y))$ is the complex correlation coefficient of the atmospheric volume. *L(·)* is a functional term accounting for the two-way path attenuation and *f(·), f'(·), f"(·)* are complex functions of the surface and volume scattering matrix elements, depending respectively on ground target, SAR received signal and atmospheric volume. Note that in the literature, the computation of δ_{co}(x,y) is simplified as it is assumed equal to $\delta_{co} = arg(\rho_{co})$ of the scattering cell in position *x,y* (Marzano et al. 2012), or ignored as in Fritz and Chandrasekar (2012).

Marzano et al. (2012) suggest a significant correlation between the SAR NRCS and the slant-integrated water contents. The SAR response seems to be mainly governed by the surface contribution σ_{SRF}, except when the two-way path within precipitation is relatively long and medium attenuation is sufficiently strong. In the latter case, the volume contribution σ_{VOL} tends to saturate and the relation between SAR NRCS and integrated water contents is much more dispersed. Moreover, the SAR response appears strongly affected by ground surface response and, to a limited extent, by the observing incident angle. The analysis at different bands suggests different SAR responses, with the X-band NRCS not being strongly influenced by frozen hydrometeors, while this is not necessarily true for Ka-band NRCS.

The polarimetric modelling of SAR response requires knowledge of the electromagnetic signatures of each water particle class affecting the wave propagation. We can define a particle class as a group, such as "moderate rain" drops or "dry snow" flakes, characterized in terms of shape, radius, PSD, temperature, composition (e.g., Marzano et al. 2008). The complexity of this approach can be simplified using an approximate but reasonable approach where the electromagnetic signature of each class is expressed through semi-empirical models of a bulk parameter, such as the water content *W(x,y,z)* (in g m^{-3}), defined for each classes. This is the approach followed in Marzano et al. (2012) at X-Band where the power-law formula has been used to model specific attenuation k_{pq}*(x,y,z)* (in dB km^{-1}), equivalent reflectivity Ze_{pq}*(x,y,z)* (in mm^6 m^{-3}), differential phase K_{co}*(x,y,z)* (in ° km^{-1}), modulus and argument of the co-polar correlation coefficient ρ_{co}*(x,y,z)* (adim). A typical parametric expression has the form of $k_{pq}(x,y,z) = a_{pq}W(x,y,z)^{b_{pq}}$.

18.3.2 Example of Precipitation-Affected SAR Scene

The model proposed in Sect. 18.3.1 can be used in order to numerically simulate the SAR response for a given scene. This requires a SAR ground response model and simulations of atmospheric water particle distributions. Realistic clouds are difficult to retrieve from in situ and remote measurements and, in this respect, synthetic clouds can be simulated more easily by cloud-resolving models. For sensitivity analysis, canonical clouds with a rectangular shape on the x-z plane and stratified in the vertical direction, composed by 1 or 2 uniform constituents (e.g., clouds,

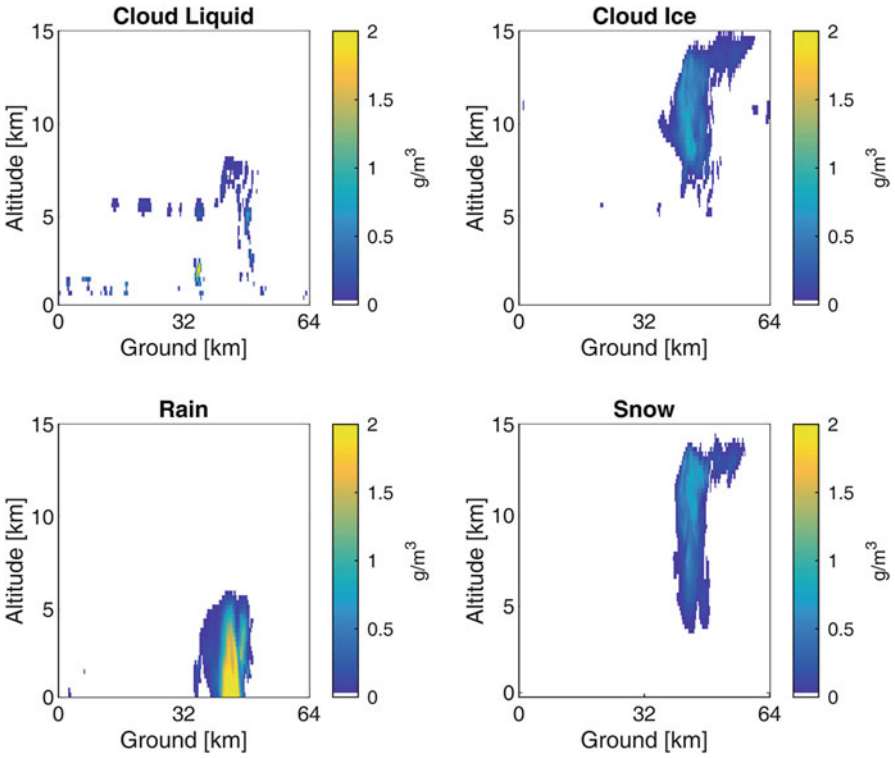

Fig. 18.5 Example of System for Atmospheric Model (SAM) vertical slice for a Compact Medium Single Cell cloud. Values indicate water content W in g m^{-3} of the simulated distributions of snow, rain, ice and cloud particles

moderate rain drops or dry snowflakes), can be also employed, as in Weinman and Marzano (2008) and Marzano and Weinman (2008).

Clouds can be simulated using the Weather Research and Forecasting (WRF) model (Michalakes et al. 2005) or the System for Atmospheric Model (SAM) Cloud Resolving Models (CRMs), as well as other Numerical Weather Prediction (NWP) models. SAM is a high-resolution (250 m) model, which simulates the 3-D water content distribution (g m^{-3}) of several kinds of hydrometeors, both precipitating (snow, graupel and rain) and non-precipitating (cloud ice, cloud liquid) (Blossey et al. 2007). A simulated SAM vertical section is given in Fig. 18.5 as an example.

A relatively simple surface target within the SAR response model is represented by bare soil. The Semi-Empirical Model (SEM) of Oh et al. (2002) allows simulation of the complete SAR polarimetric response of a realistic bare soil with a root mean square (RMS) height (k_s), a correlation length (k_l) and a volumetric soil moisture content (m_v). The simulation of Fig. 18.6 uses 1.5 cm, 5.0 cm and 0.25 cm^3 cm^{-3} as values of the three parameters, respectively. Other effective surface targets, representing many other targets and their combination, are represented by canonical targets including spheres, cylinders and dihedrals. Their combination may represent

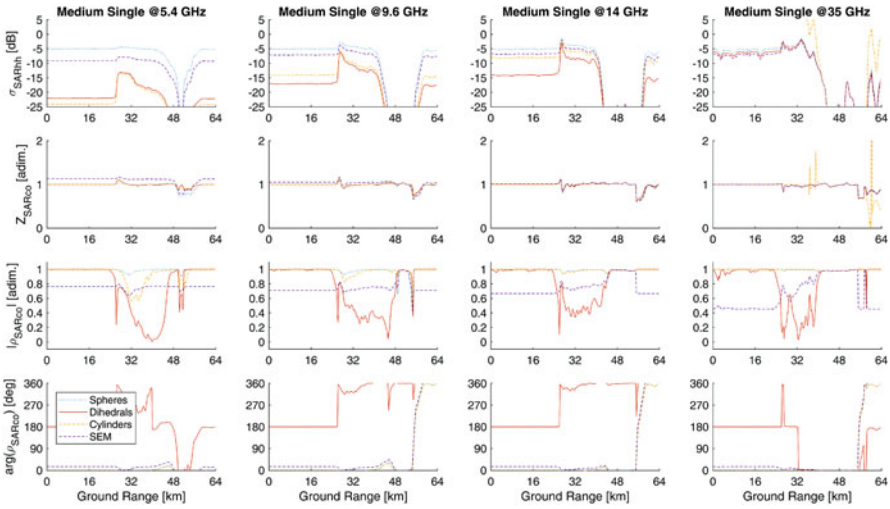

Fig. 18.6 SAR simulated response in terms of normalized Radar cross section σ_{SARhh} (horizontal transmitted and received), co-polar ratio Z_{SARco} and complex correlation coefficient ρ_{SARco} for the SAM realistic cell of Fig. 18.5. Four SAR frequencies are evaluated (5.4, 9, 14 and 35 GHz). Considered background are Spheres, Dihedrals, Cylinders, and a semi-empirical bare soil scattering model (SEM)

many natural targets according to the Freeman-Durden polarimetric decomposition (e.g., Cloude 2010). Their scattering matrix in BSA (BackScatter Alignment) convention is reported in Ulaby and Elachi (1990). The simulation of Fig. 18.6 considers spheres of 0.3 m, dihedrals of 0.025 m and cylinders of 0.030 m and 0.002 m radius, at 45° rotation. Note that NRCSs are function of target dimensions, differently from target complex correlation coefficients that are independent of dimension. In this simplified scenario, canonical targets are supposed to fill the ground scene, one target per ground cell.

Fig. 18.6 shows an example of realistic SAR responses in the presence of precipitation, for different ground targets and frequency using the model of Sect. 18.3.1. For NRCS the signal is sensitive to precipitation and frequency, as well as the precipitation pattern described in Sect. 18.3.1. At C band ground targets could be easily recognized, while at Ka band their response is similar; on the other hand, Ka-band response appears more sensitive to ice (the small peak at around km 48). Polarimetry can give useful information only at C Band. The interpretation of the complex correlation coefficient is more difficult, even if the volumetric effects is present in all bands as well as the sensitivity to different targets. The dihedral-type surface always allows the detection of clouds, whereas sphere-type surface rarely permit it. In terms of phase, the presence of a cloud introduces a significant phase rotation.

18.4 SAR Precipitation Retrieval Techniques

In order to convert X-SAR measurements into near-surface rain-rate *R(x,y)* (in mm h^{-1}), it is necessary to apply an inversion algorithm, such as the ones proposed in Marzano and Weinman (2008) and Weinman and Marzano (2008), starting from the intuition of Pichugin and Spiridonov (1991). Other easier approaches have been proposed, based on the difference (in dB) between the background NRCS $\sigma_{pp}^{0ground}(x,y)$ and the retrieved NRCS $\sigma^{0}_{SARpp}(x,y)$:

$$\Delta\sigma_{SARdB}(x,y) = \sigma_{pp}^{0ground}(x,y) - \sigma^{0}_{SARpp}(x,y) \tag{18.7}$$

Note that $\Delta\sigma_{SARdB}$ is usually positive for rainfall observations and tends to be negative for significant backscattering effects due to edge effects from the upper rain-cloud, as discussed in Sect. 18.3.

18.4.1 Data Pre-processing

X-Band SAR products, distributed by space agencies, differ in their ground resolution and areal extent, usually with an inverse relation, depending on the observing method (e.g., Ulaby and Long 2014). Usually Spotlight, Stripmap or Scansar modes are available, whereas SAR products can vary with the processing level. Using the COSMO-SkyMed notation (but similar to TerraSAR-X), the Single-look Complex Slant (SCS) outputs are the basic product available for users. Multilook Ground Detected (MGD) products are obtained through a further processing where the focused SCS is detected, radiometrically equalized and projected in range-azimuth. Further data processing envisages the correction for ellipsoid (Geocoded Ellipsoid Corrected, GEC) or terrain (Geocoded Terrain Corrected, GTC) and consequent projection on a cartographic reference system (Fritz and Eineder 2013; ASI 2009). SCS, MGD, GEC and GTC are usually indicated as Level-1 products.

For X-SAR precipitation estimation the GTC product can be used, directly dowloadable from the archives or self-produced from a SCS product using a proper processing tool (such as ENVI-SARSCAPE®). GTC product has a reduced speckle, due to 6-look averaging and approximately a square resolution on the ground of about 18×18 m^2 with a pointing knowledge error of less than 20 m. Both Stripmap and Scansar acquisition modes are suitable for precipitation analysis. The Stripmap mode has a ground coverage of about 30×30 km^2 with a resolution of about 15 m/pixel, whereas Scansar has a coverage of 200×200 km^2 with a resolution of about 30 m/pixel. These numbers refer to CSK, but they are similar in TSX. With respect to the polarization, the horizontally transmitted and horizontally received (HH) signal is preferable, being more sensitive to raindrop oblate shapes.

Several of the proposed SAR-based retrieval methods require a calibration with ground measurements. Doppler weather radar data, which allows relatively wide

coverage, continuous monitoring and a suitable range resolution, is the most suitable one. The overlapping SAR/WR data is affected by the difference in acquisition geometry and frequency band (Fritz and Chandrasekar 2010). Weather radar co-polar horizontally-polarized (HH) reflectivity factor Z can be converted into rain rates using empirical relationships which generally have the form of a power law. The suggested retrieval relation for the rainfall field $R_{WR}(x,y)$ in the x-y horizontal plane is:

$$\widehat{R}_{WR}(x,y) = \left[\frac{Z(x,y)}{a_n}\right]^{1/b_n} \tag{18.8}$$

with $a_n = 300$ and $b_n = 1.4$ for S-band NEXRAD and $a_n = 200$ and $b_n = 1.6$ for a standard Marshall-Palmer formula where R is in mm h^{-1} and Z is in linear units mm^6 m^{-3} (e.g., Bringi and Chandrasekar 2001). For Z corresponding to 59.1 dBZ (such as the case presented in Sect. 18.2), the NEXRAD Z-R and Marshall-Palmer yield R of about 283 and 180 mm h^{-1}, respectively. Strictly speaking, it is not correct to invert a statistical relation Z-R to get R-Z as in (18.8) due to different error minimization; however, this approximation is a common practice in operational radar meteorology.

In order to make SAR observation comparable with WR data, both WR and X-SAR images have to be co-registered and X-SAR images degraded through an appropriate moving-average filter at the resolution of about 0.5-km size and down-sampled at about 0.5 km ground resolution. This resolution is an upper-limit estimate consistent with the effective resolution of SAR data processing applied to incoherent moving targets such as precipitation (Marzano et al. 2010).

18.4.2 Regressive Empirical Algorithm (REA)

An effective model for radar precipitation analysis is the power-law expression to estimate of the rain-rate profile $R_{REA}(x,y)$ (in mm h^{-1}), expressed by:

$$\widehat{R}_{REA}(x,y) = a_e[\Delta\sigma_{SARdB}(x,y)]^{b_e} \tag{18.9}$$

where X-band $\Delta\sigma_{SARdB} \geq 0$ and the empirical coefficients a_e and b_e may be geographically and climatologically dependent as it happens for WRs in terms of reflectivity and rain-rate. The X-SAR side-viewing geometry introduces a characteristic pattern of the observed NRCS due to the increasing attenuation path as the incident radar ray moves within the precipitation cell from near to far ranges (e.g., Weinman and Marzano 2008). This deformation is such that the X-SAR tends to underestimate rainfall intensity at the near-range edges and to overestimate it at the far-range edges with an apparent broadening of the rainfall footprint. In order to take these geometrical effects into account, Eq. (18.9) can be modified by introducing a

factor $f_G(x)$ that accounts for the location of a pixel with respect to the edge cell. For heavy rainfall intensity, the model of (18.9) tends to underestimate the volumetric backscattering contribution σ^0_{VOLhh}, but this effect may be partially corrected by a first-order approach. The derived formulation of (18.9), proposed in Marzano et al. (2011) and called Modified Regression Empirical Algorithm (MREA), is:

$$\widehat{R}_{MREA}(x) = \begin{cases} \left[\dfrac{\Delta\sigma_{SARdB}(x) + b_v \Delta\sigma_{SARdB}(x)^{c_v}}{a}\right]^{\frac{1}{b}} \left[\dfrac{1}{x - x_0}\right]^{c_e} & x_0 + \epsilon \leq \mathrm{x} \leq x_0 + \mathrm{w} \\ 0 & \text{otherwise} \end{cases} \tag{18.10}$$

where the parameters a, b, b_v, c_v and c_e are empirical coefficients. Using WR reflectivities Z, Eq. (18.8) with Marshall-Palmer coefficients and corresponding SAR $\Delta\sigma_{SARdB}$ with an average background $\sigma_{hh}^{0ground} = -7.9$ dB, estimated coefficients are, respectively, 0.0089, 2.4595, 0.1216, 3.8979 and −0.0230 through a linear regression (Marzano et al. 2011). In (18.10) the along-track variable y has been omitted, since the formual is intended for across-track corrections only. The parameter x_0 is the near-range edge of the rain cloud with w its estimated across-track width. The parameter ε in (18.10) is introduced to prevent the singularity in $x = x_0$ and is usually equal to few pixels in the ground range. Eq. (18.10) applies to all the X-SAR pixels where $\Delta\sigma_{SARdB} \geq 1$ taking into account the $\sigma_{hh}^{0ground}$ background uncertainty.

Applying (18.10) to the Hurricane Gustav case of Sect. 18.2, a quantitative analysis of the error with respect to WR-based estimates shows that the correlation coefficient is 0.75, the error bias −0.66 mm h^{-1}, the root mean square error (RMSE) 22.28 mm h^{-1} and the Fractional RMSE (FRMSE) of about 0.98 (where FRMSE is defined as the ratio between estimation RMSE and root-mean-square value of R_{WR} over the whole dataset).

18.4.3 Probability Matching Algorithm (PMA)

A second approach, described in Marzano et al. (2010), employs a probability matching approach over a given target area (Calheiros and Zawadzki 1987). Once estimated the probability density function $p_{WR}(R_{WR})$ of WR-based rain rate RWR, and the probability density function $p_{SAR}(\Delta\sigma_{SARdB})$ of measured X-SAR differential NRCS $\Delta\sigma_{SARdB}$, the PMA method can be simply written as follows:

$$\int_{R_t}^{\widehat{R}_{PMA}} p_{WR}(R_{WR})dR_{WR} = \int_{\Delta\sigma_{dBt}}^{\Delta\sigma_{SARdB}} p_{SAR}(\Delta\sigma_{SARdB})d\Delta\sigma_{SARdB} \tag{18.11}$$

where R_t and $\Delta\sigma_{dBt}$ are rain-rate and differential σ_{SARdB} lower threshold values (e.g., equal to 0.1 mm h^{-1} and 0.5 dB, respectively). The integrals in (18.11) represent a probability (or cumulative distribution function) and if computed for increasing values of the extremes, yield an expression for PMA:

$$\widehat{R}_{PMA}(x,y) = f_{PM}(\Delta\sigma_{SARdB}(x,y)) \tag{18.12}$$

where f_{PM} is a functional which can be either implemented as a look-up table of RPMA and NRCS records or as a polynomial regressive curve. Applying PMA to the case of Sect. 18.2, yields an estimated mean error of 3.1 mm h^{-1}, an RMSE of about 13.2 mm h^{-1} and a correlation coefficient of 0.64.

18.5 Applications

18.5.1 Improving SAR Retrieval Using Background Estimation

The MREA methodology, described in Sect. 18.4.2, requires the knowledge of background NRCS in the absence of precipitating clouds. Moreover, MREA applies to the entire scene, including flooded areas, permanent water bodies and orographic shadows. These limitations can lead to severe estimation errors or misinterpretations of the scene. Improvements to MREA estimations can arise from a pre-processing step to select only areas affected by precipitations and trying to estimate the clear-sky background NRCS of these areas.

Pulvirenti et al. (2014) propose the classification methodology indicated as SAR Images Dark Object Classifier (SIDOC) that allows the differentiation of "water surfaces" from areas affected by precipitation, both appearing dark in X-SAR imagery. Water surfaces may include both permanent water bodies, such as lakes or rivers, and flooded areas and, in this respect, SIDOC shows its usefulness in both detecting areas affected by precipitations and in detecting flooded areas. SIDOC uses several ancillary data, such as Digital Elevation Model (DEM), static land cover and Local Incident Angle (LIA) maps. SIDOC consist of several steps, summarized in Fig. 18.7.

The SIDOC first step detects low backscatter areas in the input image, using a supervised Split Based Approach (SBA) and fuzzy logic that lead to determining a mean threshold, more or less suitable for the whole scene. Output of this step is a segmented map, in which the detected areas are distinguished and labelled as contiguous pixels, and a raw classification map, where pixel with high LIA (that clearly cannot be plain surfaces) are distinguished from the others. In the SIDOC second step, the remaining pixel are processed to extract shape features, such as area,

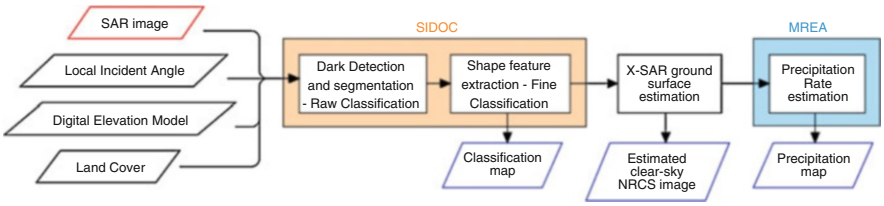

Fig. 18.7 Flowchart of the procedure described in Mori et al. (2016) for detecting flooded and cloud areas in X-SAR images and estimating the relative precipitation rate

perimeter and complexity (weighted ratio between area and perimeter): these features and fuzzy logic (together with land cover) are used to distinguish flooded areas from areas affected by precipitations.

In order to produce precipitation maps, two further steps are necessary (Mori et al. 2016). The first one consists of estimates the X-SAR ground surface response for those pixels detected as dark by SIDOC. The reconstructed $\sigma_{pp}^{0ground}$ is estimated as the mean value of the pixel near the outer border of the cloudy ones, belonging to the same land cover class and not affected by cloud or water effects. This realistic cloud-free image of the observed scene is then ingested in the MREA precipitation estimation procedure.

18.5.2 Statistical Approaches for Retrieval Validation

X-SAR precipitation detection and estimation errors should be ideally verified through ground-truth data of the analyzed area at the same time and at a similar resolution as the SAR acquisition. Unfortunately, this goal can rarely be achieved, due to the SAR high spatial resolution and relative wide coverage area and SAR near instantaneous acquisition time. A good compromise is available through the use of ground-based weather radars, that ensure a wide and uniform coverage, at a comparable ground resolution. WR volume acquisition time is quite long (about 5 min to complete a volume production) as compared to SAR, causing possible misalignments between the two data series. Moreover, the two acquisition geometries, the image formation and often the scanning frequency are quite different, resulting in another source of error. Note that WR precipitation real-time rain products can be affected by numerous sources of errors such as wet radome, spatial variability of particle size distribution, and system miscalibration (e.g., Bringi and Chandrasekar 2001).

Statistical approaches can be also considered for SAR-based retrieval analysis. The first and second order statistics of these errors can be evaluated (e.g., Stein et al. 2002). First-order statistics indicates a comparison of the spatial distribution of the retrieved rain values regardless the spatial organization of the retrieved rain fields. For this purpose, we can use the Complementary Cumulative Distribution Function (CCDF) defined as follows:

$$CCDF(X_{th}) = 1 - P(X(\mathbf{s}) > X_{th}) \quad \forall s \in D \tag{18.13}$$

In (18.13) P denotes probability, X_{th} is a threshold, D the spatial domain where the rain retrieval is carried out and $X(s)$ is a variable sampled at spatial and temporal position $s = (x,y,t)$. Second-order statistics characterizes the spatial correlation structure of the rain fields, describing the spatial variability of the variable under investigation at different spatial scales. In this respect, we can use a semi-variogram $\gamma_X(\boldsymbol{l})$ of the variable X, defined as:

$$\gamma_X(l) = \frac{1}{2}\left\langle |X(\boldsymbol{s}+\boldsymbol{l}) - X(\boldsymbol{s})|^2 \right\rangle_s \tag{18.14}$$

where l is the lag distance and s a generic position. These statistical approaches allow a comparison between WR and X-SAR data in terms of precipitation structure even though it reduces the SAR precipitation map to the resolution of the WR (Mori et al. 2016).

18.5.3 Case Study

The whole processing and validation chain of Sects. 18.5.1 and 18.5.2 is applied in Mori et al. (2016) to a couple of COSMO-SkyMed case studies. We have selected one of these cases as an application example, also for the geographical, spatial and instrumental differences with respect to the example of Sect. 18.2. The selected case is a CSK Ping-Pong acquisition over Italy (Voghera area), which occurred on 7 July 2007 at 05:18 UTC during a mid-latitude intense precipitation. The area is centered at 44.99°N – 8.94°E and covers 30 × 30 km^2 (Fig. 18.8).

Only the SCS HH channel has been processed in ENVI-SARSCAPE® in order to produce a calibrated multilooked product at 20-m pixel resolution together with DEM correction using SRTM data and UTM projected using WGS84 ellipsoid. Ground WR data are C-Band Vertical Maximum Intensities (VMI, in dBZ) obtained by the Italian national mosaic, with an acquisition frequency of 15 min and a ground resolution of about 1 km^2.

The precipitation maps, derived from SAR and WR data, are shown in Fig. 18.9. The land cover, used by SIDOC, is the Corine Land Cover (CLC) 2012, ensuring a minimum spatial resolution of 25 ha/100 m and 15 classes (at Level-II). The SAR map has been filtered with a texture filter and degraded to WR resolution in order to extract the map feature. WR precipitation map has been obtained using the standard Marshall-Palmer formula. Even if the SAR is sensitive only to moderate-to-intense precipitations areas, the geographic correspondence between WR and SAR precipitation map is fairly good with a displacement mainly due to the significant time difference between the two acquisitions (Fig. 18.10). In terms of accuracy, the mean error is -2.64 mm h^{-1} and RMSE is 15.78 mm h^{-1}. The CCDF comparison in Fig. 18.10 shows a tendency to overestimation, mainly due to the sensitivity of X-SAR to the intense portion of the rain event (leading to select only a part of the WR retrievals).

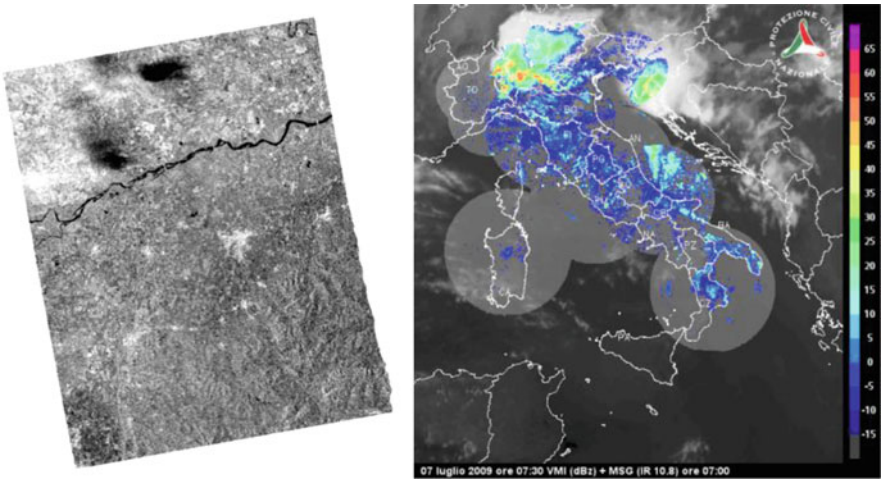

Fig. 18.8 Voghera case study. Left image is a geocoded quicklook of the CSK acquisition (at 05:18 UTC). Right figure shows the corresponding Italian National Mosaic Vertical Maximum Intensities (VMI) at 05:30 UTC (~15 min acquisition time); the ellipse approximately encloses the case study area. (Adapted from Mori et al. 2017b)

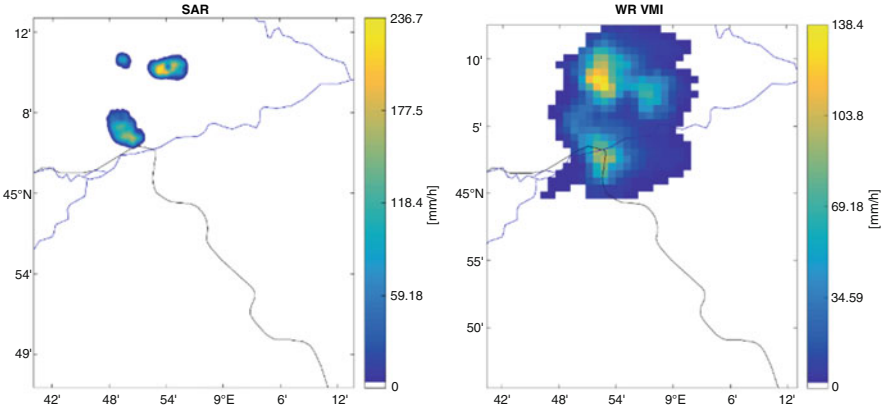

Fig. 18.9 Precipitation maps for the case study of Fig. 18.8. Left map is obtained from X-SAR data with the procedure of Sect. 18.5.1 (filtered and smoothed to WR resolution), right map is obtained by WR VMI data and a Marshall-Palmer formula. (Adapted from Mori et al. 2017b)

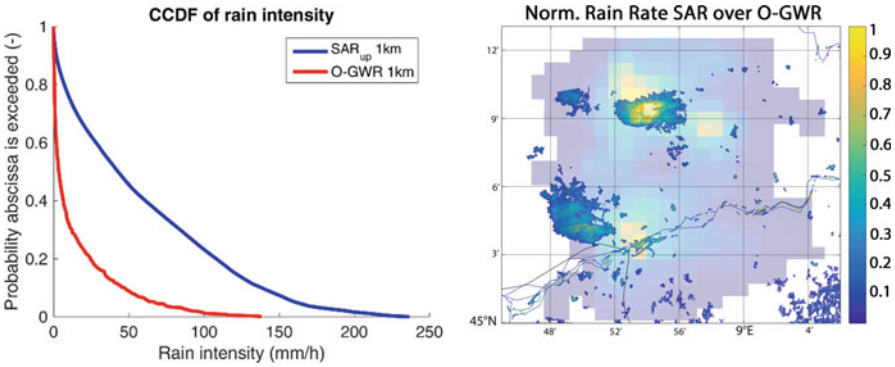

Fig. 18.10 Right plot shows the analysis of the position error between the WR precipitation map (shaded background) and the SAR one (foreground) for the case study of Fig. 18.8. Values have been normalized to the maximum of the dataset. Note that the WR data precedes the SAR data by ~12 min. Left plot shows Complementary Cumulative Distribution Function (CCDF) for the same case study. Blue lines represent SAR data degraded at WR resolution (1000 m); red lines represent WR data. (Adapted from Mori et al. 2017b)

18.6 Conclusion

Hydrometeorological applications can represent an appealing goal for spaceborne SAR missions, especially if high spatial resolution is requested. Forward and inverse models for SAR precipitation retrieval at X-band have been presented and discussed in this chapter. The SAR use at C band for flood monitoring is well established, but SAR observations can be also exploited for detecting marine winds and hurricanes. The use of Ku and Ka-band SARs for cryosphere applications has been also proposed, as in the CoRe-H2O mission concept (ESA 2012), but these SAR frequencies can be also exploited for precipitating cloud observation.

Spaceborne SARs can ensure a global coverage whose orbit duty cycle can be improved by satellite constellations, such as for COSMO-SkyMed, or operating in quasi-continuous acquisition mode, such as for Sentinel-1 satellites. Their ground spatial resolution remains unparalleled by other satellite microwave instruments. A multi-frequency SAR system can probe precipitating clouds with high-frequency sensors sensitive to stratiform rainfall and low-frequency sensors capable to sensing more intense near-surface precipitation. Most of the work to date has focused on rainfall retrievals over land while retrievals over the ocean are a future objective for X-SAR rain estimation at high spatial resolution. SAR slant-viewing geometry and precipitation retrieval processing still present several open issues to be explored in order to refine the physical-statistical retrieval approaches.

SAR future is characterized by the proposal of new space mission concepts and technologies. Recent studies exist for a geostationary SAR (e.g., Monti Guarnieri and Hu 2016) with possible hydrometeorological applications. The increasing of swath width without losing spatial resolution is under investigation by means of High Resolution Wide Swath (HRWS) SARs. Other researches explore the

feasibility and opportunity of SAR operating at Ka band for single pass interferometry, but also addressing the atmospheric influence. The KydroSAT mission concept (Mori et al. 2017b) proposes a SAR space mission entirely devoted to hydrology and cryology. KydroSAT mission concept foresees a miniaturized fully-digital SAR at Ku and Ka band (KydroSAR), specifically devoted to detecting and estimating atmospheric precipitation and surface snow; its baseline includes dual-polarization capability, high orbit duty cycle (>75%), flexible ground resolution (5–150 m), and a large variable swath (50–150 km), doubled by formation of two mini-satellites both carrying a KydroSAR. Moreover, the KydroSAT mission concept foresees the along-track convoy with the COSMO-SkyMed and SAOCOM SAR platforms, allowing the observation of the same scene at L, X, Ku and Ka bands. The challenging requirements of this architecture require the development of new technologies such as Digital Beam Forming and direct digital-to-radiofrequency conversion, which are current frontiers in SAR research. These candidate missions can effectively contribute and extend the capability to observe the precipitating clouds at high resolution, according to the principles and techniques discussed in this chapter.

References

Alpers, W., & Melsheimer, C. (2004) Rainfall. In: C. R. Jackson, & J. R. Apel (Eds.), *Synthetic Aperture Radar marine user's manual* (pp. 353–372). US Department of Commerce, NOAA. Available at http://www.sarusersmanual.com/, last accessed 15 Oct 2018.

ASI. (2009). *COSMO-SkyMed SAR products handbook rev. 2*. Available at http://www.e-geos.it/products/pdf/csk-product%20handbook.pdf, last accessed 15 Oct 2018.

Atlas, D., & Moore, R. K. (1987). The measurement of precipitation with synthetic Aperture Radar. *Journal of Atmospheric and Oceanic Technology, 4*, 368–376. https://doi.org/10.1175/1520-0426(1987)004<0368:TMOPWS>2.0.CO;2.

Baldini, L., Roberto, N., Gorgucci, E., Fritz, J. P., & Chandrasekar, V. (2014). Analysis of dual polarization images of precipitating clouds collected by the COSMO SkyMed constellation. *Atmospheric Research, 144*, 21–37. https://doi.org/10.1016/j.atmosres.2013.05.010.

Blossey, P. N., Bretherton, C. S., Cetrone, J., & Khairoutdinov, M. (2007). Cloud-resolving model simulations of KWAJEX: Model sensitivities and comparisons with satellite and radar observations. *Journal of the Atmospheric Sciences, 64*, 1488–1508. https://doi.org/10.1175/JAS3982.1.

Bringi, V. N., & Chandrasekar, V. (2001). *Polarimetric doppler weather radar, principles and applications*. Cambridge,. 536 pp: Cambridge University Press. https://doi.org/10.1017/CBO9780511541094.

Calheiros, R. V., & Zawadzski, I. I. (1987). Reflectivity rain-rate relationships for radar hydrology in Brazil. *Journal of Climate and Applied Meteorology, 26*, 118–132. https://doi.org/10.1175/1520-0450(1987)026<0118:RRRRFR>2.0.CO;2.

Cloude, S. R. (2010). *Polarisation – applications in remote sensing*. Oxford : Oxford University Press, Scholarship Online. https://doi.org/10.1093/acprof:oso/9780199569731.001.0001.

Danklmayer, A., Doring, B. J., Schwerdt, M., & Chandra, M. (2009). Assessment of atmospheric propagation effects in SAR images. *IEEE Transactions on Geoscience and Remote Sensing, 47*, 3507–3518. https://doi.org/10.1109/TGRS.2009.2022271.

Doviak, R. J., & Zrnić, D. S. (1993). *Doppler radar and weather observations*. San Diego: Academic, 562 pp, ISBN:978-0-12-221422-6.

Durden, S. L., Haddad, Z. S., Kitiyakara, A., & Li, F. K. (1998). Effects of non-uniform beam filling on rainfall retrieval for the TRMM precipitation radar. *Journal of Atmospheric and Oceanic Technology, 15*, 635–646. https://doi.org/10.1175/1520-0426(1998)015<0635:EONBFO>2.0.CO;2.

Ebert, E. E., Janowiak, J. E., & Kidd, C. (2007). Comparison of near-real-time precipitation estimates from satellite observations and numerical models. *Bulletin of the American Meteorological Society, 88*, 47–64. https://doi.org/10.1175/BAMS-88-1-47.

ESA. (2012). CoReH2O - Report for mission selection - an earth explorer to observe snow and ice. ESA SP-1324-2. http://esamultimedia.esa.int/docs/EarthObservation/SP1324-2_CoReH2Or.pdf, last accessed 15 Oct 2018

Ferrazzoli, P., & Schiavon, G. (1987). Rain-induced modification of SAR performance. *Advances in Space Research, 7*, 269–272. https://doi.org/10.1016/0273-1177(87)90323-1.

Fritz, J. P., & Chandrasekar, V. (2010). Simultaneous observations and analysis of severe storms using polarimetric X-band SAR and ground-based weather radar. *IEEE Transactions on Geoscience and Remote Sensing, 48*, 3622–3637. https://doi.org/10.1109/TGRS.2010.2048920.

Fritz, J. P., & Chandrasekar, V. (2012). A fully polarimetric characterization of the impact of precipitation on short wavelength synthetic Aperture Radar. *IEEE Transactions on Geoscience and Remote Sensing, 50*, 2037–2048. https://doi.org/10.1109/TGRS.2011.2170576.

Fritz, T., & Eineder, M. (Eds.) (2013) TerraSAR-X Ground segment. Basic product specification document. TX-GS-DD-3302, Issue 1.9. Available at https://sss.terrasar-x.dlr.de/docs/TX-GS-DD-3302.pdf, last accessed 15 Oct 2018.

Fulton, R. A., Breidenbach, J. P., Seo, D.-J., Miller, D. A., & O'Bannon, T. (1998). The WSR-88d rainfall algorithm. *Weather and Forecasting, 13*, 377–395. https://doi.org/10.1175/1520-0434(1998)013<0377:TWRA>2.0.CO;2.

Hou, A. Y., Kakar, R. K., Neeck, S., Azarbarzin, A. A., Kummerow, C. D., Kojima, M., Oki, R., Nakamura, K., & Iguchi, T. (2014). The Global Precipitation Measurement mission. *Bulletin of the American Meteorological Society, 95*, 701–722. https://doi.org/10.1175/BAMS-D-13-00164.1.

Jordan, R. L., Huneycutt, B. L., & Werner, M. (1995). The SIR-C/X SAR synthetic Aperture Radar system. *IEEE Transactions on Geoscience and Remote Sensing, 33*, 829–839. https://doi.org/10.1109/36.406669.

Kummerow, C., Barnes, W., Kozu, T., Shiue, J., & Simpson, J. (1998). The Tropical Rainfall Measuring Mission (TRMM) sensor package. *Journal of Atmospheric and Oceanic Technology, 15*, 809–817. https://doi.org/10.1175/1520-0426(1998)015<0809:TTRMMT>2.0.CO;2.

Landuyt, L., van Wesemael, A., Schumann, G. J., Hostache, R., Verhoest, N. E. C., & van Coillie, F. M. B. (2018). Flood mapping based on synthetic Aperture Radar: An assessment of established approaches. *IEEE Transactions on Geoscience and Remote Sensing*. https://doi.org/10.1109/TGRS.2018.2860054.

Li, X. (Ed.). (2017). *Hurricane monitoring with Spaceborne synthetic Aperture Radar*. Singapore: Springer, 396 pp, ISBN:978-981-10-2893-9.

Marzano, F. S., & Weinman, J. A. (2008). Inversion of spaceborne X-band synthetic Aperture Radar measurements for precipitation remote sensing over land. *IEEE Transactions on Geoscience and Remote Sensing, 46*, 3472–3487. https://doi.org/10.1109/TGRS.2008.922317.

Marzano, F. S., Mori, S., & Weinman, J. A. (2010). Evidence of rainfall signature on X-band synthetic Aperture Radar measurements over land. *IEEE Transactions on Geoscience and Remote Sensing, 48*, 950–964. https://doi.org/10.1109/TGRS.2009.2034843.

Marzano, F. S., Mugnai, A., & Turk, F. J. (2002). Precipitation retrieval from spaceborne microwave radiometers and combined sensors. In F. S. Marzano & G. Visconti (Eds.), *Remote sensing of atmosphere and ocean from space: Models, instruments and techniques* (pp. 107–126). Dordrecht: Kluwer Academic Publ, ISBN:1-4020-0943-7.

Marzano, F. S., Scaranari, D., Vulpiani, G., & Montopoli, M. (2008). Supervised classification and estimation of hydrometeors using C-band dual-polarized radars: A Bayesian approach. *IEEE Transactions on Geoscience and Remote Sensing, 46*, 85–98. https://doi.org/10.1109/TGRS.2007.906476.

Marzano, F. S., Mori, S., Montopoli, M., & Weinman, J. A. (2012). Modeling polarimetric response of spaceborne synthetic Aperture Radar due to precipitating clouds from X to Ka band. *IEEE Transactions on Geoscience and Remote Sensing, 50*, 687–703. https://doi.org/10.1109/TGRS.2011.2163942.

Marzano, F. S., Mori, S., Chini, M., Pulvirenti, L., Pierdicca, N., Montopoli, M., & Weinman, J. A. (2011). Potential of high-resolution detection and retrieval of precipitation fields from X-band spaceborne synthetic Aperture Radar over land. *Hydrology and Earth System Sciences, 15*, 859–875. https://doi.org/10.5194/hess-15-859-2011.

Masunaga, H., Satoh, M., & Miura, H. (2008). A joint satellite and global cloud- resolving model analysis of a Madden-Julian oscillation event: Model diagnosis. *Journal of Geophysical Research, 113*, D17210. https://doi.org/10.1029/2008JD009986.

Matrosov, S. Y., Kropfli, R. A., Reinking, R. F., & Martner, B. E. (1999). Prospects for measuring rainfall using propagation differential phase in X- and Ka-radar bands. *Journal of Applied Meteorology, 38*, 766–776. https://doi.org/10.1175/1520-0450(1999)038<0766:PFMRUP>2.0.CO;2.

Melsheimer, C., Alpers, W., & Gade, M. (1998). Investigation of multifrequency/ multipolarization radar signatures of rain cells derived from SIR-C/X-SAR data. *Journal of Geophysical Research, 103*, 18867–18884. https://doi.org/10.1029/98JC00779.

Michalakes, J., Dudhia, J., Gill, D., Henderson, T., Klemp, J., Skamarock, W., & Wang, W. (2005). The weather research and forecast model: Software architecture and performance. In W. Zwieflhofer & G. Mozdzynski (Eds.), *Use of high performance computing in meteorology* (pp. 156–168). Singapore: World Scientific. https://doi.org/10.1142/9789812701831_0012.

Monti Guarnieri, A., & Hu, C. (2016). Geosynchronous and geostationary SAR: Face-to-face comparison. In *Proceedings of EUSAR 2016: 11th European conference on synthetic Aperture Radar*, Hamburg, Germany, 6–9 June.

Moore, R. K., Mogili, A., Fang, Y., Beh, B., & Ahamad, A. (1997). Rain measurement with SIR-C/X-SAR. *Remote Sensing of Environment, 59*, 280–293. https://doi.org/10.1016/S0034-4257(96)00147-2.

Mori, S., Montopoli, M., Pulvirenti, L., Marzano, F. S., & Pierdicca, N. (2016). Detection and quantification of precipitations signatures on synthetic Aperture Radar imagery at X band. In *Proceedings of SPIE 10003, SAR image analysis, modeling, and techniques XVI*, 1000306, Edinburgh, UK, 18 Oct. https://doi.org/10.1117/12.2241943.

Mori, S., Marzano, F. S., & Pierdicca, N. (2017a). Atmospheric distortions of spaceborne SAR polarimetric signatures at X and Ka-band. In *8th Int. Workshop on science and applications of SAR polarimetry and polarimetric interferometry (POLinSAR)*, Frascati, 23–27 January 2017.

Mori, S., Marzano, F. S., Pierdicca, N., Bombaci, O., Giancristofaro, D., Macelloni, G., Lemmetyinen, J., Giudici, D., & Poghosyan, A. (2017b). KydroSAT: A Ku/Ka band Synthetic Aperture Radar space mission concept for high-resolution mapping of hydrometeorological parameters. In *Proceedings of SPIE 10426, Active and passive microwave remote sensing for environmental monitoring XVI*, 1042603, Warsaw, Poland, 11–14 Sept. https://doi.org/10.1117/12.2277993.

Oh, Y., Sarabandi, K., & Ulaby, F. T. (2002). Semi-empirical model of the ensemble-averaged differential Muller matrix for microwave backscattering from bare soil surfaces. *IEEE Transactions on Geoscience and Remote Sensing, 40*, 1348–1355. https://doi.org/10.1109/TGRS.2002.800232.

Pichugin, A. P., & Spiridonov, Y. G. (1991). Spatial distributions of rainfall intensity recovery from space radar images. *Soviet Journal of Remote Sensing, 8*, 917–932.

Pulvirenti, L., Marzano, F. S., Pierdicca, N., Mori, S., & Chini, M. (2014). Discrimination of water surfaces, heavy rainfall and wet snow using COSMO-SkyMed observations of severe weather events. *IEEE Transactions on Geoscience and Remote Sensing, 52*, 858–869. https://doi.org/10.1109/TGRS.2013.2244606.

Quegan, S., & Lamont, J. (1986). Ionospheric and tropospheric effects on synthetic Aperture Radar performance. *International Journal of Remote Sensing, 7*, 525–539. https://doi.org/10.1080/01431168608954707.

Refice, A., D'Addabbo, A., & Capolongo, D. (2018). *Flood monitoring through remote sensing*. Cham: Springer, 208 pp, ISBN:978-3-319-63959-8.

Roberto, N., Baldini, L., Facheris, L., & Chandrasekar, V. (2014). Modelling COSMO-SkyMed measurements of precipitating clouds over the sea using simultaneous weather radar observations. *Atmospheric Research, 144*, 38–56. https://doi.org/10.1016/j.atmosres.2014.01.016.

Skofronick-Jackson, G., Petersen, W. A., Berg, W., Kidd, C., Stocker, E. F., Kirschbaum, D. B., Kakar, R., Braun, S. A., Huffman, G. J., Iguchi, T., Kirstetter, P.-E., Kummerow, C., Meneghini, R., Oki, R., Olson, W. S., Takayabu, Y. N., Furukawa, K., & Wilheit, T. (2017). The Global Precipitation Measurement (GPM) mission for science and society. *Bulletin of the American Meteorological Society, 98*, 1679–1695. https://doi.org/10.1175/BAMS-D-15-00306.1.

Stein, A., van der Meer, F. D., & Gorte, B. (Eds.). (2002). *Spatial statistics for remote sensing*. Dordrecht: Springer, 260 pp, ISBN:978-0-306-47647-1.

Ulaby, F. T., & Elachi, C. (1990). *Radar polarimetry for geoscience applications*. Boston: Artech House, 350 pp, ISBN:9780890064061.

Ulaby, F. T., & Long, D. G. (2014). *Microwave radar and radiometric remote sensing*. Ann Arbor: University of Michigan Press, 984 pp, ISBN:978-0-472-11935-6.

Weinman, J. A., & Marzano, F. S. (2008). An exploratory study to derive rainfall over land from spaceborne synthetic Aperture Radars. *Journal of Applied Meteorology and Climatology, 47*, 562–575. https://doi.org/10.1175/2007JAMC1663.1.